

# The Virgo High-Resolution CO Survey: VI. Gas Dynamics and Star Formation Along the Bar in NGC 4303

Jin KODA

*California Institute of Technology, MS 105-24, Pasadena, CA 91125, USA  
 and National Astronomical Observatory, Mitaka, Tokyo, 181-8588  
 koda@astro.caltech.edu*

and

Yoshiaki SOFUE

*Institute of Astronomy, The University of Tokyo, Mitaka, Tokyo, 181-0016  
 sofue@ioa.s.u-tokyo.ac.jp*

(Received 2005 December 27; accepted 2006 February 13)

## Abstract

We present CO interferometer observations of the barred galaxy NGC 4303 (M61). This galaxy has a strong gas concentration at the central region and prominent offset ridges at the leading sides of the bar. Sharp velocity gradients are apparent across the ridges. The brightness temperature in the ridges is low, indicating the existence of unresolved molecular clouds. Additionally, an analysis of the newborn stellar clusters revealed in *HST* images suggests that the parent molecular clouds had masses of  $10^{4-6} M_{\odot}$ . The observed shear velocity gradient across the ridges is too small to break up giant molecular clouds. Therefore, the clouds are likely to survive passage through the ridges. We discuss a cloud orbit model in a bar potential for understanding the gas distribution, dynamics, and star formation in NGC 4303. The model reproduces the narrow offset ridges and sharp velocity gradients across the ridges, although no shock is associated with the ridges. We discuss cloud-cloud collisions (and close interactions) as a possible triggering mechanism for star formation. The newborn stellar clusters in NGC 4303 are located predominantly at the leading sides of the offset ridges. Cloud orbits are densely populated in the region where the clusters are found, suggesting a high collisional frequency and possibly a high rate of triggered star formation. Cloud-based dynamics is less dissipative than smooth hydrodynamic models, possibly extending the timescales of gas dynamical evolution and gas fueling to central regions in barred galaxies.

**Key words:** galaxies: individual(NGC 4303) – galaxies: ISM – galaxies: kinematics and dynamics

## 1. Introduction

Despite numerous observational and theoretical studies, the nature of interstellar medium (ISM) gas dynamics remains uncertain (Combes 1996). The dynamical response of the gas depends significantly on whether the ISM is a continuous hydrodynamic fluid or a set of discrete molecular clouds. The hydrodynamic fluid produces shocks along spiral arms or bars in galaxies, while the molecular clouds could ballistically pass the spiral/bar structures without encountering a shock. Such differences must change not only the dynamical response of the gas (e.g. shock, dissipation), but also the evolution timescale (e.g. gas inflow) and star formation.

The Galactic ISM is concentrated in discrete molecular clouds (Scoville, Sanders 1987), and supports the dynamics of slightly collisional clouds. Individual molecular clouds are rarely resolved in external galaxies; however, there is a general belief that only continuous hydrodynamic models could reproduce the narrow gas/dust lanes observed in barred galaxies, since hydrodynamic fluids easily produce narrow shock lines along bars. We demonstrate that an alternative scenario, cloud-based gas dynamics, also reproduces the narrow gas distribution and

associated gas kinematics in bars.

The large-scale distribution of star-forming regions and young stars provides a clue to understanding gas dynamics. Star formation triggered by hydrodynamic shocks would be localized in narrow shocked regions. Cloud-cloud interactions could potentially occur everywhere in galactic disks and cause star formation. We compare CO observations of the barred galaxy NGC 4303 to the cloud-based gas dynamics model. The cloud-based model naturally explains the distribution of young stellar clusters.

Figure 1 shows the *B* and *H $\alpha$*  band images of NGC4303; most HII regions are associated with outer spiral arms, but almost no apparent *H $\alpha$*  emission is found in the bar. Similar trends have been found in many other barred galaxies (Downes et al. 1996; Regan et al. 1996; Garcia-Barreto et al. 1996; Sheth et al. 2000; 2002). The absence of active star formation in bars is often attributed to strong shear velocity in the bar (Reynaud, Downes 1998). However, we point out below that the shear in NGC 4303 is too small to break up dense molecular clouds.

NGC 4303 hosts remarkable central activity: a nuclear secondary bar (Colina, Wada 2000), prominent UV emission around the secondary bar (Colina et al. 1997), and an active galactic nucleus (AGN; Colina, Arribas 1999).

It has been a prime example of the starburst-AGN connection (Colina et al. 1997; Colina, Arribas 1999; Colina, Wada 2000; Jiménez-Bailón et al. 2003). Schinnerer et al. (2002) discussed gas fueling toward the nucleus due to the secondary bar based on their CO data. Our focus, however, is on the gas dynamics and star formation around the offset ridges in the primary bar.

We describe the observations and data in §2, and results in §3. We introduce a cloud-orbit model in the bar and show its ability to reproduce the observed CO distribution and velocity structure (§4). We discuss star formation along the bar using the cloud-based model (§5). Conclusions are summarized in §7. This paper is the sixth in a series on the Virgo CO survey at the Nobeyama Millimeter Array (Sofue et al. 2003a; 2003b; 2003c; Onodera et al. 2004; Nakanishi et al. 2005).

— Figure 1 —

— Table 1 —

## 2. Observational Data

### 2.1. NMA CO(1-0) Observations

We made aperture synthesis observations of the Virgo cluster galaxy NGC 4303 in the CO  $J = 1 - 0$  line emission using the Nobeyama Millimeter Array (NMA). The observations were made between 1999 December and 2000 February with a single pointing center at  $(\alpha_{1950}, \delta_{1950}) = (12^{\text{h}}19^{\text{m}}21^{\text{s}}.6, +4^{\circ}45'3''.0)$ . Six 10 m telescopes provide the FWHP of about  $65''$  at 115 GHz. We used three available array configurations (AB, C, and D configurations). The typical system noise temperature was about 400K in single sideband. Digital spectro-correlators (Okumura et al. 2000) have two spectroscopic modes; we used the mode covering 512 MHz ( $1331\text{ km s}^{-1}$ ) with the 2 MHz ( $5.2\text{ km s}^{-1}$ ) resolution. We observed the quasar 3C273 every 20 minutes for gain and bandpass calibrations. The absolute flux of 3C273 was measured against Uranus and/or available flux-known quasars; it was 14.2Jy for 1999 December, and 11.4Jy for 2000 January and February. The uncertainties in the flux scale are about 20%.

Raw visibility data were calibrated for pass-band response and complex gain variation with the NRO/UVPROC-II package (Tsutsumi et al. 1997). The data were binned to 4 MHz resolution. Each channel data was deconvolved with the CLEAN procedure using the NRAO/AIPS package. We applied both natural and uniform weightings for the visibility data and obtained  $2''.4$ - and  $1''.3$ -resolution maps, respectively. We refer the  $2''.4$ -resolution map as “map”. The parameters of the observation and data cubes are given in Table 2 and 3, respectively.

— Table 2 —

— Table 3 —

Figures 2 shows zeroth- and first-moment maps, and synthesized beam map. Figure 3 and 4 show the velocity

channel maps and position-velocity (PV) diagrams, respectively. Primary beam attenuation is not corrected for these maps. In the synthesized beam map (Figure 2), prominent sidelobes run in the north-south direction and are aligned with the observed emission distribution. These sidelobes made the deconvolution less obvious; we arranged restricted CLEAN boxes and checked that the 2nd- and 3rd-order sidelobes are also reduced successfully in the deconvolution. We estimated the recovered flux by comparing our data with a single-dish observation at the FCRAO 14 m telescope (Kenney, Young 1988). Our map recovers 97% of the total flux in the central  $45''$  (with the uncertainties of 20%) .

— Figure 2 —

— Figure 3 —

— Figure 4 —

### 2.2. Supplied Optical/Near-IR Data

We obtained optical and near-infrared images from the archives and literature through the NASA/IPAC Extragalactic Database (NED): the  $B$ -band image from the Digitized Sky Survey,  $\text{H}\alpha$ -image (Figure 1 and 5) from Koopmann, Kenney, and Young (2001), and  $K$ -band image (Figure 5) from Moellenhoff and Heidt (2001). We also obtained  $HST$  images in the F450W and F814W-filters (P.I. Smartt) through the HST archive at the Canadian Astronomy Data Center (CADC). The F450W and F814W images are shown in Figure 6.

The astrometry of the  $B$ - and  $\text{H}\alpha$ -band images was determined using the USNO-A2.0 catalog (Zacharias et al. 2000). The  $K$ -band and  $HST$  images do not contain enough cataloged stars; we shift the central compact emission peak in each image to the dynamical center (§3.3). The centroids of compact sources across these images coincide with those in the lower-resolution  $B$ -band image. The uncertainty of the absolute position in each image is about  $0''.5$ .

— Figure 5 —

— Figure 6 —

## 3. Results

Figure 2 shows two remarkable features in the gas distribution: (1) a central concentration within  $r \sim 10''$  (780 pc, hereafter the central disk), and (2) offset ridges extending from the central concentration out to  $r \sim 30''$  (2.3 kpc). The gas is rotating clockwise, assuming trailing spiral arms. Below, we obtain the parameters of the gas disk and discuss the two features.

### 3.1. Global CO Properties

Figure 7 shows the radial profile of the CO integrated intensity  $I_{\text{CO}} V \cos(i)$  and cumulative flux  $S_{\text{CO}}$ . Corrections for the primary beam response and inclination were applied. We adopted the position angle  $\text{P.A.} = -45^\circ$ ,

inclination  $i = 30^\circ$  (see §3.2), and the CO-to-H<sub>2</sub> conversion factor  $X_{\text{CO}} = 1.8 \times 10^{20} \text{cm}^{-2} [\text{K km s}^{-1}]^{-1}$  (Dame et al. 2001). The surface density is almost constant at  $\sim 500 M_\odot \text{pc}^{-2}$  from the center to  $r \sim 4''$  (310 pc), and decreases exponentially with a scale length of  $\sim 4.5''$  (350 pc). The total detected gas mass is  $8.4 \times 10^8 M_\odot$  within the radius  $13''$  (1 kpc), and is  $1.0 \times 10^9 M_\odot$  within  $30''$  (2.3 kpc).

— Figure 7 —

### 3.2. Central Concentration

The CO emission is very concentrated in the central disk ( $r < 10''$ ) in Figure 2. The velocity field is the typical “spider diagram”. The gas is following almost pure circular rotation. Spiral arms are curling along the outer edge of the central disk (Figure 8). They are associated with slight perturbations in the velocity field at the outer edges of the central disk. We obtained kinematic parameters from the velocity-field assuming pure circular rotation. The dynamical center, position angle, inclination, and recession velocity were determined using the AIPS/GAL package (Table 4). Since the perturbations due to the spiral arms are small, the errors due to the perturbations should be small. The derived parameters are consistent with those from previous studies (Colina, Arribas 1999; Schinnerer et al. 2002).

— Figure 8 —

### 3.3. Offset Ridges

Two gas ridges run out from the central disk in the north and south directions (Figure 2). Figure 5 (*left*) compares the gas distribution (grayscale; CO image) with the stellar bar (contours; *K*-band image). The two ridges are at the leading sides of the stellar bar. This type of ridge is referred to as “offset ridges”, and is often found in barred galaxies (Ishizuki et al. 1990; Sakamoto et al. 1999; Sheth et al. 2002). The gas ridges coincide with dust lanes in Figure 6. There are gas concentrations at the outermost ends of the detected CO ridges (Figure 2), which coincide with the stellar bar ends. Such gas concentration is common in barred galaxies. Note that no primary beam correction has been applied to this map; the fluxes of these gas concentrations are therefore about 2-times larger than the contour values shown in the figure.

Sharp velocity gradients exist across the offset ridges; in the channel maps (Figure 3), the southern CO ridge shifts east (toward left) as the velocity decreases, and the northern ridge shifts west (right) as the velocity increases. The isovelocity contours run along the offset ridges in the velocity field map (Figure 2). The velocity differences across the ridges,  $\sim 4''$ , is about  $\sim 20 \text{ km s}^{-1}$  (i.e. three channels) in projection on the sky.

The typical brightness temperature is  $T_b \sim 1 \text{ K}$  along the offset ridges (Figure 3). Assuming an excitation temperature  $T_{\text{ex}} = 10 \text{ K}$  for optically-thick molecular gas (Scoville, Sanders 1987) and the cosmic microwave background temperature of  $T_{\text{CMB}} = 2.7 \text{ K}$ , the area filling factor within

the beam ( $2.4'' \sim 200 \text{ pc}$ ) is  $f \sim 0.1$ . Thus, the emission arises from unresolved clumpy structures, presumably molecular clouds. The average gas surface density in the beam is typically  $\Sigma_{\text{gas}} = 150 M_\odot \text{pc}^{-2}$ . Therefore, molecular clouds are dense with an average surface density of  $\Sigma_{\text{MC}} \sim \Sigma_{\text{gas}}/f \sim 1000 M_\odot \text{pc}^{-2}$ . This is much denser than  $170 M_\odot \text{pc}^{-2}$  for clouds in the Galactic disk (Solomon et al. 1987), but less dense than  $2500 M_\odot \text{pc}^{-2}$  for clouds in the Galactic center (Oka et al. 2001). Note that a velocity dilution might underestimate the value  $f$  by a factor of 2, although it does not affect the following discussion. The typical velocity width of the offset ridges is about  $20 \text{ km s}^{-1}$  (Figure 3), and that of molecular clouds in the Galaxy is  $9 \text{ km s}^{-1}$  (FWHM; Scoville, Sanders 1987).

### 3.4. Star Formation around Offset Ridges

Evidence of star formation (SF) around the offset ridges is inferred from many bright points in the *HST* images (Figure 6), although active SF is not obvious in the H $\alpha$  image (Figure 5 *right*). Each of the bright points is very likely a stellar cluster. Their luminosities indicate that the masses are  $10^{3-4} M_\odot$ . Assuming an extinction  $A_V = 1 \text{ mag}$  and a color excess 0.71 (Cardelli et al. 1989), the typical intrinsic color in F450W-F814W is as blue as  $-0.7 \text{ mag}$  (AB magnitude), indicating their young ages,  $\lesssim 10^7 \text{ yr}$  (see Appendix). Because of the large scatter in color ( $\pm 0.5 \text{ mag}$ ), we could not detect any significant systematic color change as a function of the distance from the ridges.

The clusters are distributed predominantly at the leading side of the gas ridges, i.e. at the downstream side assuming that the corotation radius is around the bar end. No obvious cluster is found at the opposite (upstream) side, which is especially notable for the southern ridge. Therefore, the star formation was initiated during, or after, passage of the parent molecular cloud across the offset ridges. Some clusters are found *far* from the gas ridges. The rotation timescale around the galaxy,  $10^8 \text{ yr}$ , is ten-times longer than the cluster age,  $\lesssim 10^7 \text{ yr}$ . Thus, those clusters should have been formed not *on* the ridges, but *long after* passage of the cloud across the ridges.

The conversion of molecular gas to stars in a molecular cloud is normally a very inefficient process in the Galaxy with a conversion efficiency of 0.01-0.1 (Evans, Lada 1991; Lada 1992). Consequently, the parent molecular clouds of the stellar clusters should have had masses of  $10^{4-6} M_\odot$ , which are typical for Galactic molecular clouds (Scoville, Sanders 1987).

### 3.5. Comparison with Other CO Maps

Three CO maps of NGC 4303 have been published from mm-wave interferometer observations, at the Owens Valley Radio Observatory (OVRO; Schinnerer et al. 2002), at the Nobeyama Millimeter Array (NMA; Sofue et al. 2003a, and this paper), and at the Berkeley-Illinois-Maryland Association (BIMA; Helfer et al. 2003).

The BIMA map has three-times lower sensitivity of  $\sim 47 \text{ mJy}$  and resolution of  $\sim 6''$ , but includes zero-spacing baselines (extended components) from single dish obser-

vations. It is thus good for tracing the large-scale distribution of molecular gas. The BIMA map shows significant CO emission along the outer spiral arms. The brightness is comparable between the offset ridges and spiral arms, though star formation is more active in the arms (Figure 1).

The OVRO map has similar sensitivity ( $\sim 20\text{mJy}$ ) and resolution ( $\sim 2''$ ) to our map. The CO distribution and velocity structure are consistent between the OVRO and NMA maps. The recovered flux compared with the single-dish data (Kenney, Young 1988), however, is 2-times higher in NMA than in OVRO. We compared the two data cubes<sup>1</sup>, and found that the NMA flux is  $\sim 1.4$  times larger in spectrum and  $\sim 2$  times greater in integrated intensity. The lower OVRO flux probably results from a combination of the assumed calibrator flux ( $\sim 10\text{ Jy}$  vs  $\sim 14.5\text{ Jy}$ ) and a lack of short-spacing  $uv$  coverage in the OVRO data. This difference does not affect the discussions made in this paper and in Schinnerer et al. (2002).

#### 4. Gas Dynamics in NGC 4303

We use a cloud-orbit model to interpret the gas dynamics in NGC 4303. To derive the stellar orbits in the bar, the equations of motion for a test particle are solved in a bar potential (Contopoulos, Papayannopoulos 1980; Binney, Tremaine 1987). Wada (1994) included the damping force term, “ $-2\lambda\dot{R}$ ”, in the equations of motion, the force negatively proportional to the velocity  $\dot{R}$ , and obtained the orbits of collisional gas clouds. This model has provided successful interpretations for observed barred and spiral galaxies (Sakamoto et al. 2000; Koda et al. 2002; Onodera et al. 2004). Figure 9, 10, and 11 show the model gas orbits, density and velocity field maps, and position-velocity diagrams. The gas and bar are rotating clockwise. The model is scalable; it fits to NGC 4303 when the units are  $300\text{pc}$  in length and  $160\text{kms}^{-1}$  in velocity. The pattern speed and bar radius (corotation radius) are scaled to  $53\text{kms}^{-1}\text{kpc}^{-1}$  and  $3\text{kpc}$ , respectively, which is consistent with the bar radius in Figure 1.

— Figure 9 —

##### 4.1. Offset Ridges and Central Spirals

Figure 10 shows the projection of the gas orbits with a position angle of  $-45^\circ$  and an inclination of  $30^\circ$  (Table 4). The stellar bar runs vertically. The density map (*middle*) reproduces the observed offset ridges and the central spiral arms in Figure 2. To calculate the density, we used the timescale of passage along the orbit as a weighting function. The offset ridges and central spiral arms appear to be dense for two reasons: (1) the gas orbits are crowded at the leading side of the bar, and (2) passing the apocenter of an orbit takes longer time than passing the pericenter.

There is a common expectation that the offset ridges are produced by hydrodynamic shock; the tangential orbital velocity of the gas is damped by the shock, and the gas

falls toward the galactic center along the offset ridges. The orbit model, however, indicates that *no shock is required to form the dense and narrow offset ridges*. In fact, the sharp turns are apparent in the *rotating* frame with the bar (Figure 9 *left*), but disappear in the rest frame (*right*). The tangential velocity becomes very close to the rotation speed of the bar on the offset ridges, which produces the apparent turns. This fact is particularly important when the orbits of young stars born recently in molecular clouds are discussed. We note that this argument does not exclude the possibility of shock as a secondary effect.

— Figure 10 —

The velocity field (Figure 10 *right*) is consistent with the observations (Figure 2 *middle*). The major axes of elongated gas orbits are aligned with that of the galaxy at the central disk, and therefore, the isovelocity contours are similar to those of pure circular rotation (spider diagram). Slight deviations from pure circular rotation are apparent along the spiral arms on the central disk; we found similar deviations in the observed velocity field (Figure 2 *middle*). At the outer part, the isovelocity contours run along the offset ridges as found in the observations. The contours parallel to the offset ridges indicate abrupt velocity changes across the ridges, although no shock is associated.

— Figure 11 —

Figure 11 shows position-velocity (PV) diagrams with three different position angles (PA). The diagram with  $\text{PA} = -45^\circ$  corresponds to NGC 4303 and is similar to the observed one. The model reproduced the observations in space (maps) and velocity (PV diagram), indicating that the orbit model represents the gas motions in NGC 4303. The other two diagrams, i.e.  $\text{PA} = 0^\circ$  and  $-90^\circ$ , are projections from the edge-on and pole-on directions of the bar, respectively. The same gas distribution shows quite different patterns; our determination of the PA and inclination in §3.2 were suitable for NGC 4303.

##### 4.2. Cloud-cloud Collisions as a Damping Force

The damping force term “ $-2\lambda\dot{R}$ ” provides the damping timescale,  $t_{\text{damp}} = 1/\lambda$ , in which random motions decay. For the above model, we defined the damping coefficient  $\Lambda \equiv \lambda/\kappa_0 = 0.1$  as in previous studies (Wada 1994; Sakamoto et al. 2000). The orbits are insensitive to the change of  $\Lambda$  by a factor of a few (Wada 1994). We discuss its physical cause in an order-of-magnitude approximation. Assuming a constant rotation velocity  $V = 160\text{kms}^{-1}$  at a radius of  $1\text{kpc}$  as for NGC 4303, the epicyclic frequency becomes  $\kappa_0 \sim 200\text{kms}^{-1}\text{kpc}^{-1}$ . The damping timescale is then  $t_{\text{damp}} = 1/\Lambda\kappa_0 \sim 5 \times 10^7\text{yr}$  for  $\Lambda = 0.1$ .

We have shown the presence of dense molecular clouds in NGC 4303 (§3.3). The damping timescale is close to the collisional timescale of clouds calculated as follows. NGC 4303 has a gas mass of  $10^8 M_\odot$  between radii of  $1 - 2\text{kpc}$  (Figure 7). Assuming a cloud mass  $M_{\text{MC}} = 10^5 M_\odot$  and diameter  $D = 20\text{pc}$ , the surface number density of molecular clouds is  $N_{\text{MC}} = 100\text{kpc}^{-2}$ . If

<sup>1</sup> OVRO data cube was kindly provided by Eva Schinnerer.



the cloud-cloud velocity dispersion is  $\sigma = 10 \text{ km s}^{-1}$  and the galactic molecular disk is thin (2-D) in the central region, the collisional timescale between molecular clouds becomes  $t_{\text{col}} = 1/N_{\text{MC}} D \sigma \sim 4 \times 10^7 \text{ yr}$ . Close encounters would occur on a slightly shorter timescale but on the order of  $10^7 \text{ yr}$ . These are close to the damping timescale for  $\Lambda \sim 0.1$ . Cloud collisions could be the cause of the damping force.

Ram pressure from ambient gas is negligible. Using the density of the ambient gas  $\rho$ , the relative velocity between a cloud and the ambient gas  $v$ , the cloud cross section  $A$ , and the mass  $M_{\text{MC}}$ , the acceleration on the cloud is  $a_{\text{ram}} = \rho v^2 A / M_{\text{MC}}$ . The velocity difference would decay in  $t_{\text{ram}} = v / a_{\text{ram}}$ . If the ambient gas is atomic hydrogen with a density of  $1 \text{ cm}^{-3}$  and a velocity of  $v = 10 \text{ km s}^{-1}$ ,  $t_{\text{ram}} \sim 10^9 \text{ yr}$ , which is much longer than  $t_{\text{col}}$ .

#### 4.3. Shear Velocity and the Survival of Molecular Clouds

Downes et al. (1996) discussed that molecular clouds might be destroyed by strong shear around offset ridges. Assuming that the shapes and orientations of the gas orbits in Figure 10 *left* are all correct, molecular clouds have only the velocity components tangential to our line-of-sight before the ridges, and only the line-of-sight velocity components after the ridges. The velocity difference across the ridges is then  $\sim 40 \text{ km s}^{-1}$  from the observed velocity difference of  $20 \text{ km s}^{-1}$  and an inclination of  $30^\circ$ . The width of the ridge is  $\sim 300 \text{ pc}$  ( $\sim 4''$ ), and thus the velocity gradient (shear) is about  $0.13 \text{ km s}^{-1} \text{ pc}^{-1}$ .

The surface density of a molecular cloud in NGC 4303 is about  $\Sigma_{\text{MC}} = 1000 M_\odot \text{ pc}^{-2}$  (§3.3). Assuming a cloud radius  $R = 10 \text{ pc}$ , the escape velocity from the cloud,  $v_{\text{esc}} = (2\pi G \Sigma_{\text{MC}} R)^{1/2}$ , is  $16 \text{ km s}^{-1}$ . Thus, a sharp velocity gradient of  $1.6 \text{ km s}^{-1} \text{ pc}^{-1}$  is necessary to destroy the molecular cloud. This is an order of magnitude above the observed shear velocity gradient in NGC 4303. Even for some molecular clouds with lower surface densities of  $100 M_\odot \text{ pc}^{-2}$  (typical for the Galactic molecular clouds), the escape velocity is still higher than the observed shear velocity. Thus, shear is unlikely to destroy molecular clouds. *The clouds are likely to survive passage across the ridges.*

### 5. Collision-Induced Star Formation in the Bar

The existence of molecular clouds is necessary but not sufficient for star formation (Mooney, Solomon 1988; Scoville, Good 1989; Fukui et al. 1999). There is considerable evidence that cloud-cloud collisions may initiate star formation (Loren 1976; Scoville et al. 1986; Odenwald et al. 1992; Hasegawa et al. 1994). The efficiency of collisional dissipation (§4.2) also supports the cloud-based mechanism for triggering star formation. We explore the cloud-cloud collision (or close encounter) model to account for star formation.

#### 5.1. Star Formation at the Leading Side of Ridges

The damping timescale of random motions is close to the rotation timescale of  $10^8 \text{ yr}$  around the galactic cen-

ter (§4.2). Thus, the dissipation is not very effective, and newborn stars should follow similar orbits to those of the parent molecular clouds (Figure 9) within about one rotation timescale. Comparing the distribution of the young clusters (Figure 6) to the orbits (Figure 10 *left*), we find that the majority of the clusters are aligned on the outermost orbits in Figure 10. Hence, most star formation occurs at the outer ends of the offset ridges. The same consideration can be applied to other barred galaxies (see Sheth et al. 2002); the outer ends of offset ridges are the primary loci of star formation in the bars.

We discussed in §3.4 that some of the stellar clusters have large offsets from the gas ridges (Figure 6). Considering the isochrones along the orbits (Figure 12) and the young cluster ages  $\lesssim 10^7 \text{ yr}$ , they should have been born long ( $10^7 \text{ yr}$ ) after the parent clouds cross the ridges. Star formation is, therefore, triggered even after (but not before) the offset ridges. This cannot be explained by the star formation induced by galactic shocks. In Figure 9 *left*, the separation between orbits is remarkably narrow at the leading side of the ridges. The number density of clouds would therefore be larger at the leading side, and possibly result in more frequent cloud collisions (or close encounters). The collision model explains the star formation after the ridges.

— Figure 12 —

The presence of HII regions at the leading side of the ridges has been a problem for hydrodynamic models (Sheth et al. 2002). They predict that the gas loses the tangential velocity at offset shocks, and falls toward the galactic center along the offset ridges (Regan et al. 1999, see their Figure 9). If star formation occurs due to the shocks, i.e. after the tangential velocity is damped, the newborn stars should also fall *along* the offset ridges and cannot exist at their leading side (Sheth et al. 2002). The orbit model, however, naturally explains the co-motion of molecular clouds and stars, and the star-forming regions at the leading side.

Young stars are bright in UV emission for  $10^8 \text{ yr}$  after birth (Iglesias-Páramo et al 2004), which is close to the rotation timescale. If the young stars follow the gas orbits for a single rotation timescale and if the outer edges of the ridges are the primary loci of star formation, the outermost orbits in Figure 10 *left* would stand out in UV emission from young stars. This is the case for NGC 4303 in the GALEX/UV image (Gil de Paz et al. 2006 in preparation).

### 6. Cloud Model vs Hydrodynamic Model

Most hydrodynamic models assume an isothermal gas with a sound speed of  $\sim 10 \text{ km s}^{-1}$ , which is similar to the observed cloud-cloud velocity dispersions. The corresponding effective temperature is about  $10^4 \text{ K}$ , far higher than the typical kinetic temperature of molecular gas ( $\sim 10 \text{ K}$ ). Therefore, the hydrodynamic models represent not the diffuse molecular gas, but an ensemble of a significant number of molecular clouds. The difference between

the two models arises from the number of clouds being considered. Cloud-based dynamics assumes fewer clouds, and thus, would be less dissipative than smooth hydrodynamic models. The efficiency of gas fueling to galactic centers could be lower than what we expect from hydrodynamic simulations.

Obviously, there is diffuse, presumably continuous, gas around the discrete clouds. The gas is cycling between the two phases due to cloud formation, stellar feedback, ram pressure stripping of the cloud envelope, etc. This cycling would affect the gas dynamics. To discuss these effects, molecular clouds have to be resolved in galaxies with higher resolution observations (e.g. ALMA) and simulations (e.g. Wada, Koda 2001).

## 7. Conclusions

We observed the central 5 kpc of the barred galaxy NGC 4303 in the CO(1-0) line with the Nobeyama Millimeter Array. We discussed the gas distribution and dynamics, and compared them with young stellar cluster distribution in *HST* images. The main conclusions are:

1. NGC 4303 has a central gas concentration (disk) and offset ridges along its stellar bar. The central disk follows pure circular rotation with slight perturbations due to spiral arms on the disk. Sharp velocity gradients are observed across the offset ridges.

2. The brightness temperature in the  $2''.4$ -resolution map is much lower than the typical excitation temperature of molecular gas in the Galaxy. Assuming that the gas is optically thick in CO(1-0), the beam-filling factor is about 0.1, indicating the existence of dense molecular clouds ( $\sim 1000 M_{\odot} \text{ pc}^{-2}$ ) in the offset ridges.

3. The velocity gradient across the offset ridges is about  $0.13 \text{ km s}^{-1} \text{ pc}^{-1}$ . This is an order of magnitude smaller than the gradient necessary to break up existing molecular clouds. Therefore, the clouds survive after passing the offset ridges.

4. Many young stellar clusters are found in *HST* images, although star formation is not apparent in the  $\text{H}\alpha$  image. The clusters have ages of  $\lesssim 10^7 \text{ yr}$  and masses  $10^3\text{--}4 M_{\odot}$ . If the star-formation efficiency is 0.01-0.1, their parent molecular clouds should have had masses of  $10^4\text{--}6 M_{\odot}$ .

5. The young clusters are distributed predominantly at the downstream side of the offset ridges. Some of them are located far from the offset ridges and, therefore, are born long after their parent clouds pass the ridges.

6. We used a cloud orbit model to simulate the gas dynamics. The dynamics due to slightly-collisional clouds reproduces the central gas disk, narrow offset ridges, and their associated velocity structure. The offset ridges are not necessarily associated with shock.

7. The strength of viscous (damping) force is a parameter of choice in the cloud orbit model. The best-fit value gives a timescale of  $5 \times 10^7 \text{ yr}$  for the decay of random motions, which is close to the timescale of cloud-cloud collisions or close interactions in NGC 4303.

8. Cloud collisions naturally explain the formation of the young clusters far from the offset ridges. Cloud-orbits

are densely populated at the leading side of the ridges, indicating a high collision frequency and star formation.

## Appendix 1. Color Evolution of a Stellar Cluster

Figure 13 shows the model color evolution of a stellar cluster. Three photometric synthesis models are compared: Bruzual and Charlot (1993, hereafter, BC93), Fioc and Rocca-Volmerange (1999, Pegase), and Leitherer et al. (1999, Starburst99). We used the Salpeter initial mass function (IMF) with a mass range  $0.1 - 100 M_{\odot}$  for BC93, the Scalo98 IMF with a range  $0.1 - 120 M_{\odot}$  for Pegase, and the IMF having indices of 1.3 for  $0.1 - 0.5 M_{\odot}$  and 2.3 for  $0.5 - 100 M_{\odot}$  for Starburst99. The F450W-F814W color drops sharply around  $7 \times 10^6 \text{ yr}$  for all three models. The uncertainties are a factor of 2 in time and 0.1 mag in magnitude. The stellar clusters bluer than  $+0.0 \text{ mag}$  (§3.3) are, therefore, younger than  $\lesssim 10^7 \text{ yr}$  (and  $2 \times 10^7 \text{ yr}$  at the oldest).

— Figure 13 —

We thank Tsutomu Takamiya, Kotaro Kohno, Makoto Hidaka, Hiroyuki Nakanishi, and Sachiko Onodera for useful discussions and collaborations in the Virgo CO survey project. We also thank the NMA staff for their help with observations, and Keiichi Wada for fruitful discussions. J. K. thanks Ryo Kandori for helping with the data analysis, Eva Schinnerer for providing her CO data, Armando Gil de Paz and Samuel Boissier for providing their paper prior to publication, Nick Scoville and Jenny Patience for carefully reading the manuscript, and Kartik Sheth for useful comments. We thank an anonymous referee for comments, which helped to clarify the paper. J. K. was financially supported by the Japan Society for the Promotion of Science for Young Scientists. This work was partially supported by National Science Foundation under grant AST-9981546.

## References

- Binney, J., & Tremaine, S. 1987, *Galactic Dynamics* (Princeton, NJ: Princeton University Press)
- Bruzual, A. G., & Charlot, S. 1993, *ApJ*, 405, 538
- Cardelli, J. A., Clayton, G. C., & Mathis, J. S. 1989, *ApJ*, 345, 245
- Colina, L., & Arribas, S. 1999, *ApJ*, 514, 637
- Colina, L., Garcia Vargas, M. L., Mas-Hesse, J. M., Alberdi, A., & Krabbe, A. 1997, *ApJ*, 484, L41
- Colina, L., & Wada, K. 2000, *ApJ*, 529, 845
- Colina, L., Gonzalez Delgado, R., Mas-Hesse, J. M., & Leitherer C. 2002, *ApJ*, 579, 545
- Combes, F. 1996, in *ASP Conf. Ser. 91, Barred Galaxies*, ed. R. Buta, D. A. Crocker, & B. G. Elmegreen (San Francisco: ASP), 286
- Contopoulos, G., & Papayannopoulos, T. 1980, *A&A*, 92, 33
- Dame, T. M., Hartmann, D., & Thaddeus, P. 2001, *ApJ*, 547, 792
- de Vaucouleurs, G., de Vaucouleurs, A. Corwin, H. G. Jr., Buta, R. J., Paturel, G., & Fouque, P. 1991, *Third Reference Catalogue of Bright Galaxies* (Berlin: Springer)
- Downes, D., Reynaud, D., Solomon, P. M., & Radford, S. J. E. 1996, *ApJ*, 461, 186
- Evans, N. J., & Lada, E. A. 1991, in *IAU Symposium 147, Fragmentation of Molecular Clouds and Star Formation*, ed. E. Falgarone, F. Boulanger, & G. Duvert (Dordrecht: Kluwer), 293
- Ferrarese, L. et al. 1996, *ApJ*, 464, 568
- Fioc, M., & Rocca-Volmerange, B. 1997, *A&A*, 326, 950
- Fukui, Y., et al. 1999, *PASJ*, 51, 745
- Garcia-Barreto, J. A., Franco, J., Carrillo, R., Venegas, S., & Escalante-Ramirez, B. 1996, *Rev. Mex. Astron. Astrofis.*, 32, 89
- Hasegawa, T., Sato, F., Whiteoak, J. B., & Miyawaki, R. 1994, *ApJ*, 429, L77
- Helfer, T. T., Thornley, M. D., Regan, M. W., Wong, T., Sheth, K., Vogel, S. N., Blitz, L., & Bock, D. C. -J. 2003, *ApJS*, 145, 259
- Ho, L. C., Filippenko, A. V., & Sargent, W. L. W. 1997, *ApJS*, 112, 315
- Iglesias-Páramo, J., Boselli, A., Gavazzi, G., Zaccardo, A. 2004, *A&A*, 421, 887
- Ishizuki, S., Kawabe, R., Ishiguro, M., Okumura, S. K., Morita, K. -I. 1990, *Nature*, 344, 224
- Jiménez-Bailón, E., Santos-Lleó, M., Mas-Hesse, J. M., Guainazzi, M., Colina, L., Cerviño, M., & González Delgado, R. M. 2003, *ApJ*, 593, 127
- Kenney, J. D., & Young, J. S. 1988, *ApJS*, 66, 261
- Koda, J., Sofue, Y., Kohno, K., Nakanishi, H., Onodera, S., Okumura, S. K., Irwin, J. A. 2002, *ApJ*, 573, 105
- Koda, J., & Wada, K. 2002, *A&A*, 396, 867
- Koopmann, R. A., Kenney, J. D. P., & Young, J. 2001, *ApJS*, 135, 125
- Lada, E. A. 1992, *ApJ*, 393, L25
- Leitherer, C., et al. 1999, *ApJS*, 123, 3
- Loren, R. B. 1976, *ApJ*, 209, 466
- Moellenhoff, C., & Heidt, J. 2001, *A&A*, 368, 16
- Mooney, T. J., & Solomon, P. M. 1988, *ApJ*, 334, L51
- Nakanishi, H., Sofue, Y., & Koda, J. 2005, *PASJ*, 57, 905
- Nishiyama, K., & Nakai, N. 2001, *PASJ*, 53, 713
- Odenwald, S., Fischer, J., Lockman, F. J., & Stemwedel, S. 1992, *ApJ*, 397, 174
- Oka, T., Hasegawa, T., Sato, F., Tsuboi, M., Miyazaki, A., & Sugimoto, M. 2001, *ApJ*, 562, 348
- Okumura, S. K., et al. 2000, *PASJ*, 52, 393
- Onodera, S., Koda, J., Sofue, Y., & Kohno, K. 2004, *PASJ*, 56, 439
- Regan, M. W., Teuben, P. J., & Vogel, S. N. 1996, *AJ*, 112, 6
- Regan, M. W., Sheth, K., & Vogel, S. N. 1999, *ApJ*, 526, 97
- Regan, M. W., & Teuben, P. J. 2004, *ApJ*, 600, 595
- Reynaud, D., & Downes, D. 1998, *A&A*, 337, 671
- Sakamoto, K., Baker, A. J., & Scoville, N. Z. 2000, *ApJ*, 533, 149
- Sakamoto, K., Okumura, S. K., Ishizuki, S., & Scoville, N. Z. 1999, *ApJS*, 124, 403
- Schinnerer, E., Maciejewski, W., Scoville, N., & Moustakas, L. A. 2002, *ApJ*, 575, 826
- Scoville, N. Z., & Good, J. C. 1989, *ApJ*, 339, 149
- Scoville, N. Z., Sanders, D. B., & Clemens, D. P. 1986, *ApJ*, 310, L77
- Scoville, N. Z., & Sanders, D. B. 1987, in *Interstellar Processes*, ed. D. J. Hollenbach & H. A. Thronson, Jr. (Dordrecht: Reidel).
- Sheth, K., Regan, M. W., Vogel, S. N., & Teuben, P. J. 2000, *ApJ*, 532, 221
- Sheth, K., Vogel, S. N., Regan, M. W., Teuben, P. J., Harris, A. I., & Thornley, M. D. 2002, *AJ*, 124, 2581
- Sofue, Y., Koda, J., Nakanishi, H., & Hidaka, M. 2003c, *PASJ*, 55, 75
- Sofue, Y., Koda, J., Nakanishi, H., Onodera, S., Kohno, K., Tomita, A., & Okumura, S. K. 2003a, *PASJ*, 55, 17
- Sofue, Y., Koda, J., Nakanishi, H., & Onodera, S. 2003b, *PASJ*, 55, 59
- Solomon, P. M., Rivolo, A. R., Barrett, J., & Yahil, A. 1987, *ApJ*, 319, 730
- Tsutumi, T., Morita, K. -I., & Uneyama, S. 1997, in *ASP Conf. Ser. 125, Astronomical Data Analysis Software and Systems VI*, ed. G. Hunt, & H. E. Payne (San Francisco: ASP), 50
- Wada, K. 1994, *PASJ*, 46, 165
- Wada, K., & Koda, J. 2001, *PASJ*, 53, 1163
- Zacharias, N., et al. 2000, *AJ*, 120, 2131

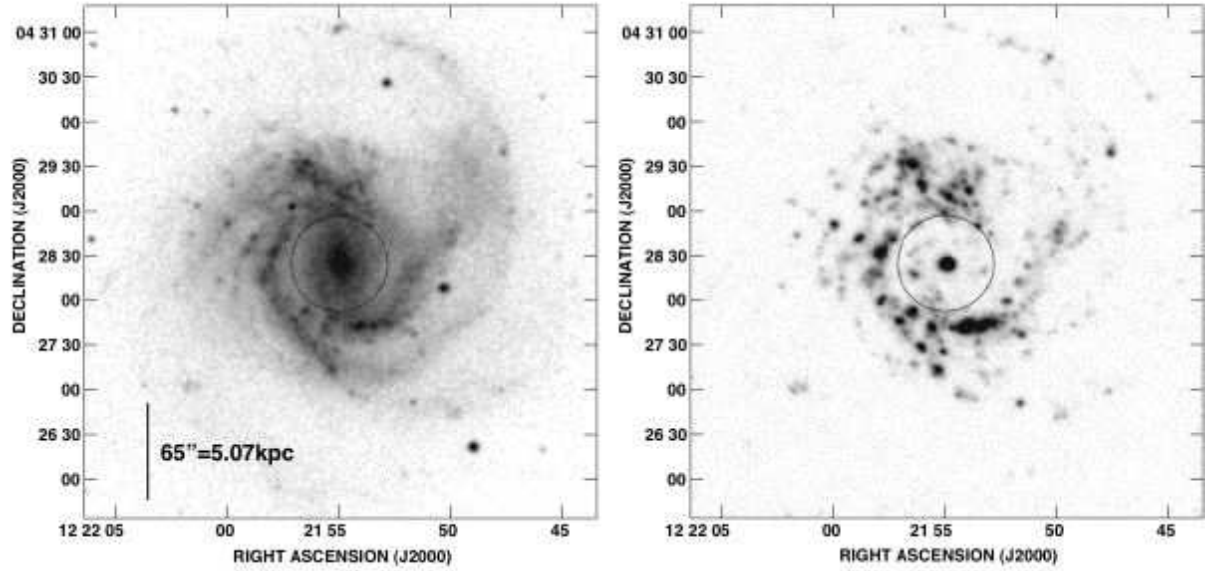


Fig. 1. *Left:*  $B$ -band image of NGC 4303 from the Digitalized Sky Survey. *Right:*  $H\alpha$  image from Koopmann, Kenney, and Young (2001). The circles represent the primary beam size of the  $^{12}\text{CO}(J=1-0)$  observations ( $65''$  HPBW).

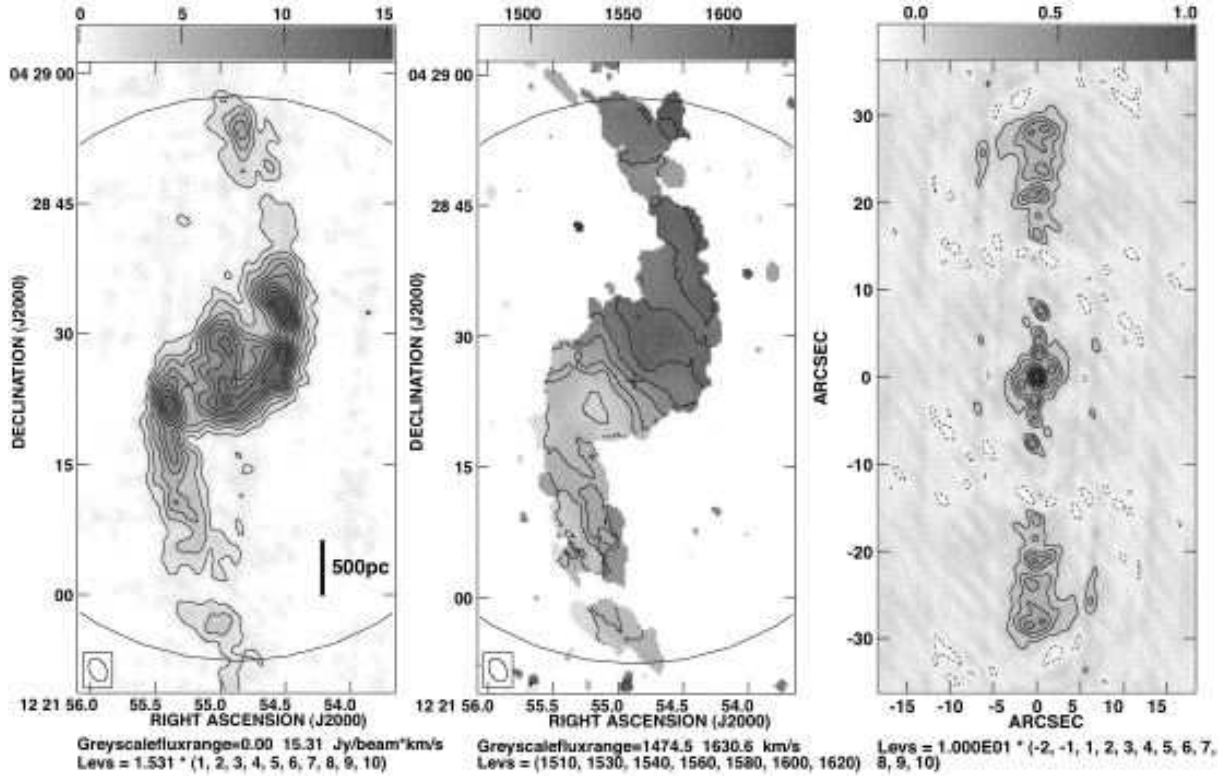
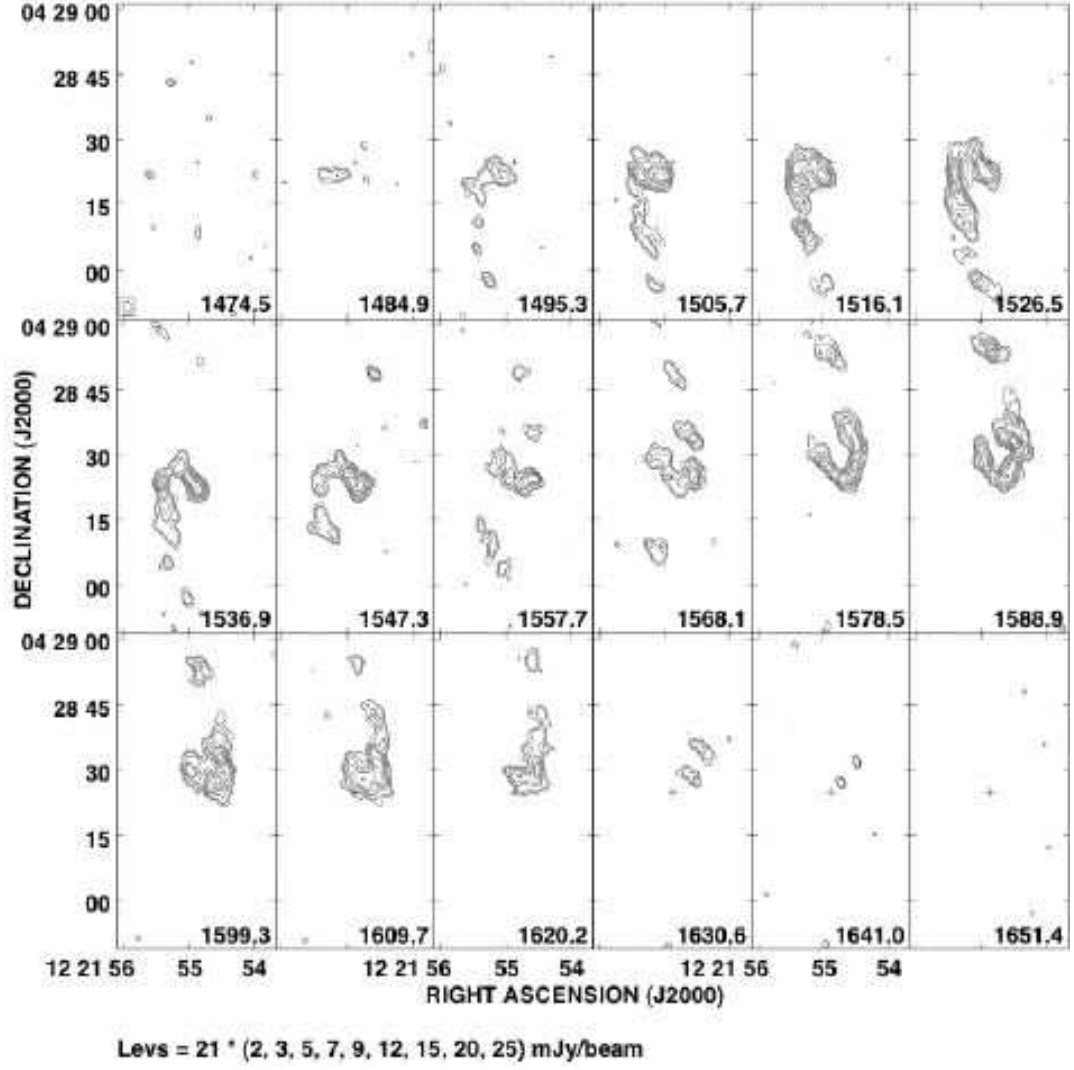
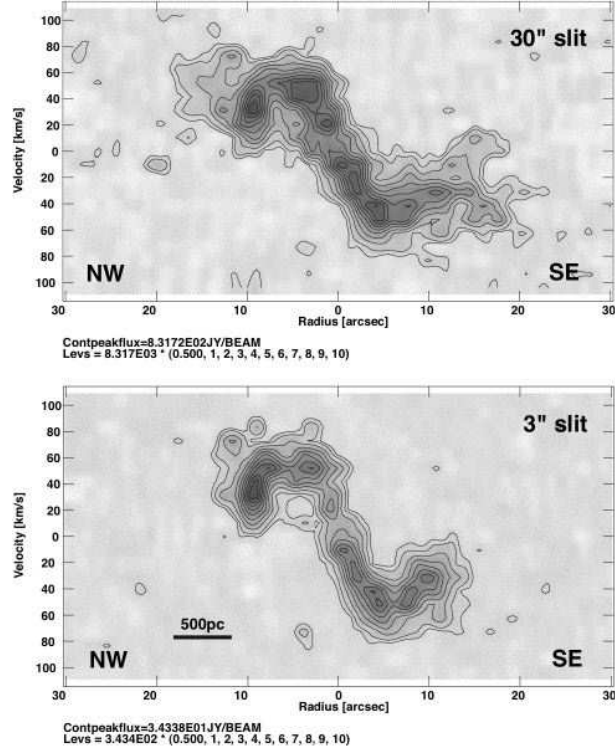


Fig. 2. CO(1-0) zeroth- and first-moment maps of NGC 4303, and synthesized beam map. A clip at the  $2\sigma$  level was used to make these maps. The circles represent the size of the primary beam. No primary beam correction was applied.





**Fig. 3.** CO(1-0) velocity channel maps of NGC 4303 in the same region as in Figure 2. The velocities at the channels are shown at the lower right corners. No primary beam correction was applied. The  $1 \text{ mJy beam}^{-1}$  corresponds to  $0.017 \text{ K}$  in brightness temperature.



**Fig. 4.** Position-velocity diagrams with  $PA = -44.45$  and slit widths of  $30''$  (*upper panel*) and  $3''$  (*lower panel*). The contours are 0.05, 0.1, 0.2, 0.3, 0.4, 0.5, 0.6, 0.7, 0.8, 0.9, 1.0 times the peak intensity.

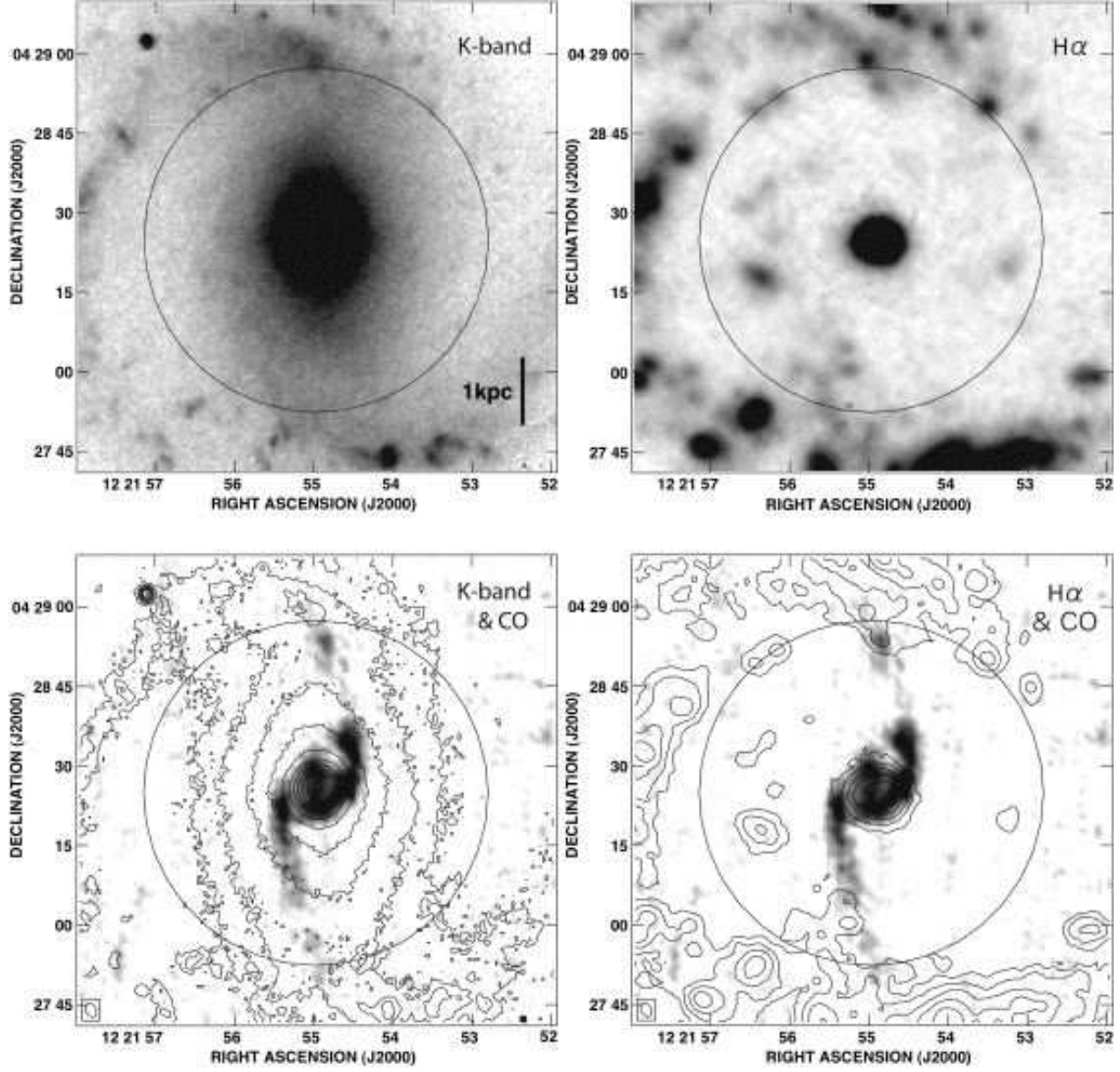


**Fig. 5.** *K*-band and  $H\alpha$  images of the central  $90'' \times 90''$  region of NGC 4303. *Upper-left:* *K*-band image. *Lower-left:* *K*-band contours on CO grayscale image. Contours are 0.008, 0.012, 0.018, 0.027, 0.041, 0.061, 0.091, 0.14, 0.21, 0.31, 0.46, 0.69, 1.0 times the peak *K*-band intensity. *Upper-right:*  $H\alpha$  image. *Lower-right:*  $H\alpha$  contours on CO grayscale image. Contours are 0.031, 0.063, 0.125, 0.25, 0.5, 1.0 times the peak  $H\alpha$  intensity. The circles represent the field-of-view (FWHM) of CO observations.

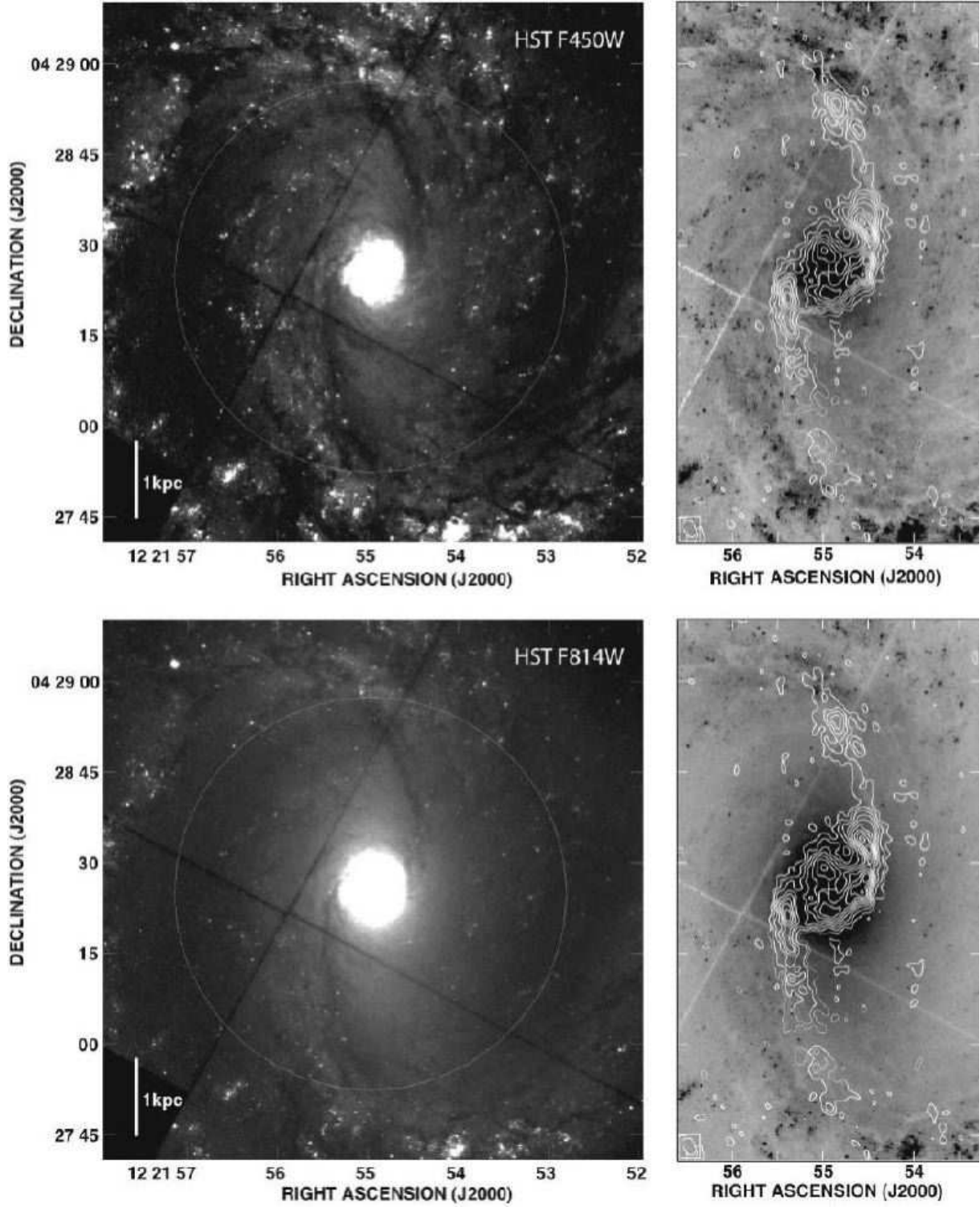


**Fig. 6.** HST images of the central  $90'' \times 90''$  region of NGC 4303, the same region covered in Figure 1. *Upper panels:* HST F450W band images. *Lower panels:* HST F814W band images. Right panels are the central vertical strips of the left images, and CO contours are overlaid. Contours are 0.1, 0.2, 0.3, 0.4, 0.5, 0.6, 0.7, 0.8, 0.9, 1.0 times the peak CO intensity. The circles represent the FoV (FWHM) of CO observation. The bright points across the images are very likely stellar clusters. They are distributed predominantly at the leading (downstream) side of the gas ridges, i.e. the eastern side of the southern ridge and the western side of the northern ridge.



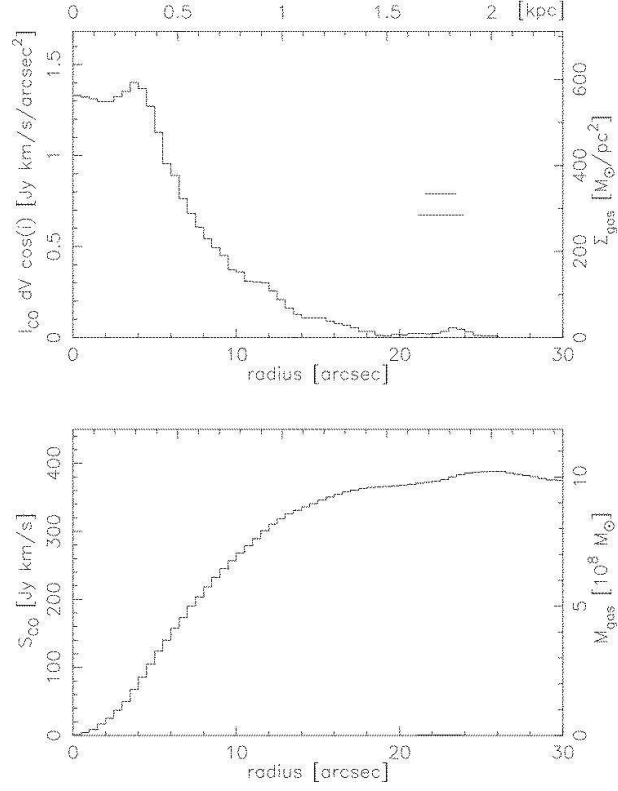


**Fig. 7.** Radial profiles of the integrated-intensity (inclination corrected). The physical scales at the top and right axes were calculated using the distance of 16.1 Mpc and a conversion factor of  $X_{\text{CO}} = 1.8 \times 10^{20} \text{ cm}^{-2} [\text{K km s}^{-1}]^{-1}$ . We assumed  $M_{\text{gas}} = 1.41 M_{\text{H}_2}$ , taking He and the other elements into account. The two horizontal lines indicate the sizes of the major and minor axes of the synthesized beam.

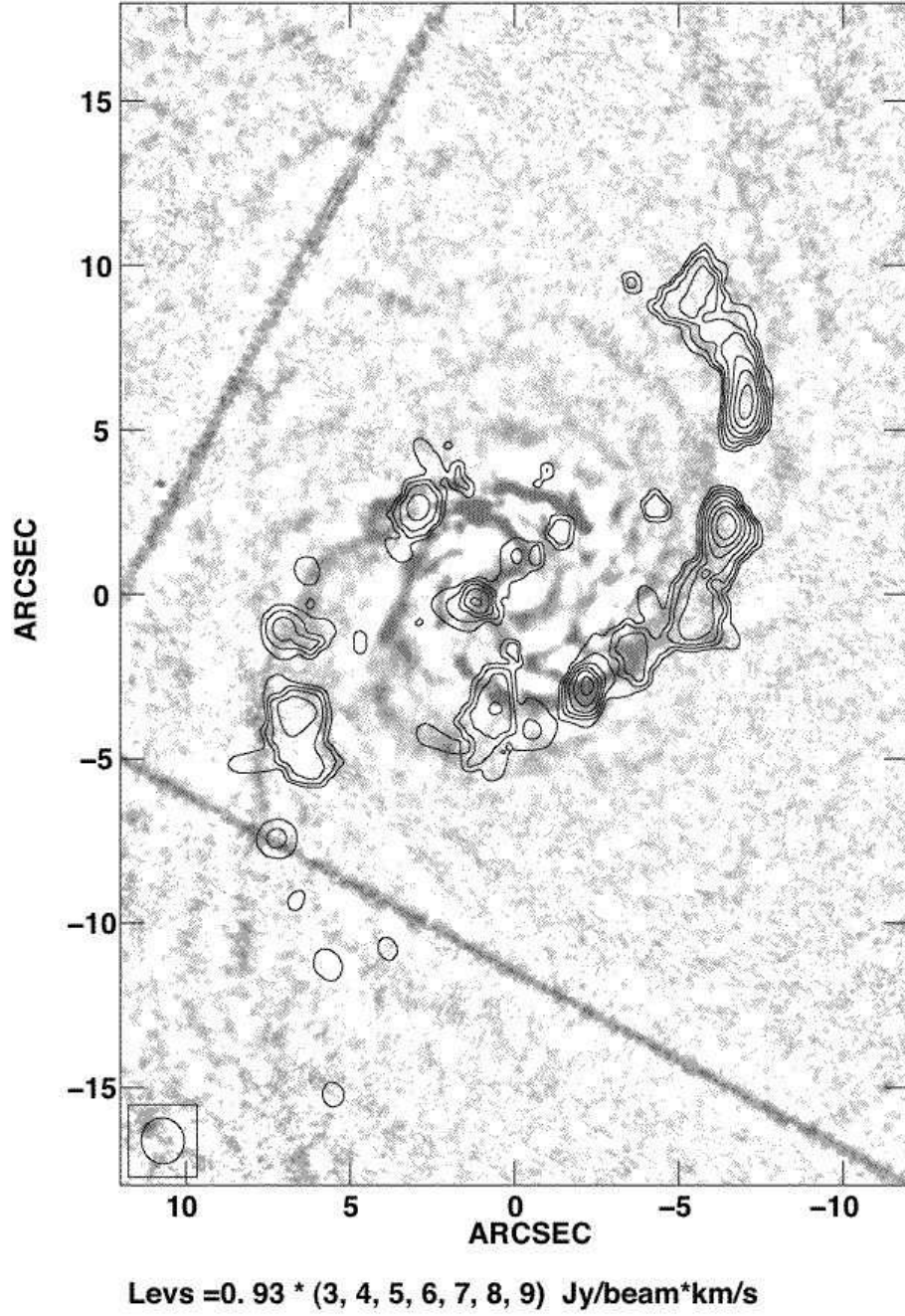


**Fig. 8.** High-resolution (uniform weighting) CO contours at the top of an unsharp-masked *HST* F814W image. The contours are 0.3, 0.4, 0.5, 0.6, 0.7, 0.8, 0.9 times the peak intensity, 0.9 Jy/beam\*km/s.

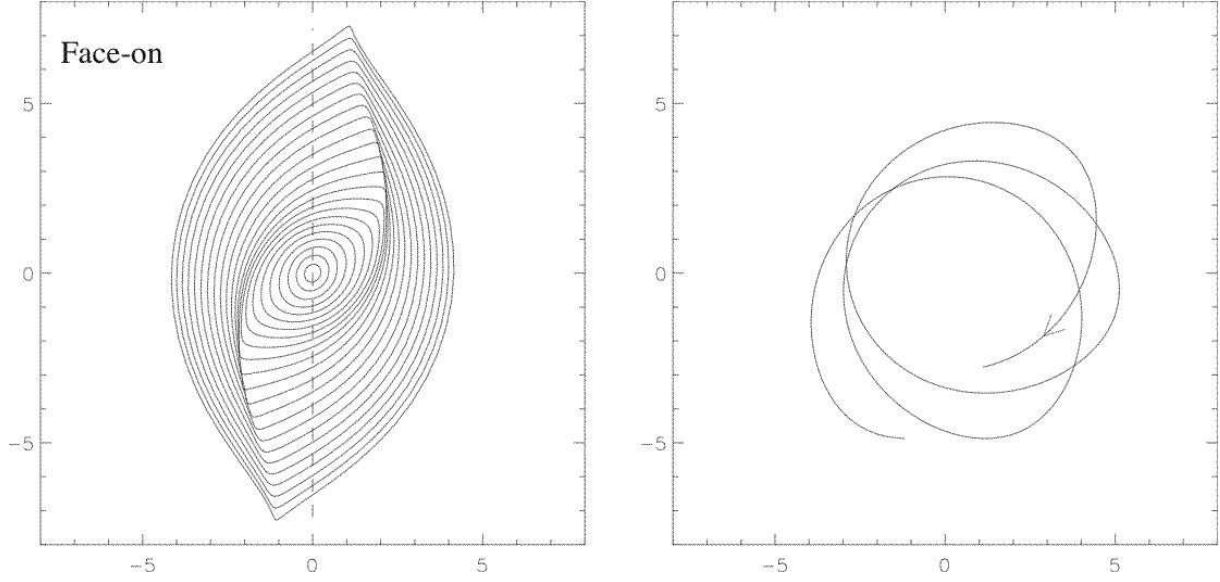


**Fig. 9.** *Left:* Gas orbits in a bar in the rotating frame with the bar (clockwise rotation). The dashed line indicates the bar direction. *Right:* An orbit in the non-rotating reference frame. The gas is rotating clockwise in both panels. We used the potential  $\Phi(R, \varphi) = (1 - \epsilon \cos 2\varphi) \frac{v_0^2}{2} \log(1 + (R/a)^2)$ , where  $a = 1$ ,  $v_0 = 1$  and  $\epsilon = 0.04$ . The pattern speed of the bar is  $\Omega_b = 0.1$ . The two inner Lindblad resonances and the corotation radii are  $R_{\text{ILR}} = 1.1, 2.0$ , and  $R_{\text{CR}} = 9.9$ , respectively. Assuming a bar length of 6 kpc ( $77''$ ) and rotational velocity of  $160 \text{ km s}^{-1}$  at the radius of 3 kpc for NGC 4303, the units of the model become  $a = 300 \text{ pc}$  ( $3''.8$ ),  $v_0 = 160 \text{ km s}^{-1}$ , and  $\Omega_b = 53 \text{ km s}^{-1} \text{ kpc}^{-1}$ .

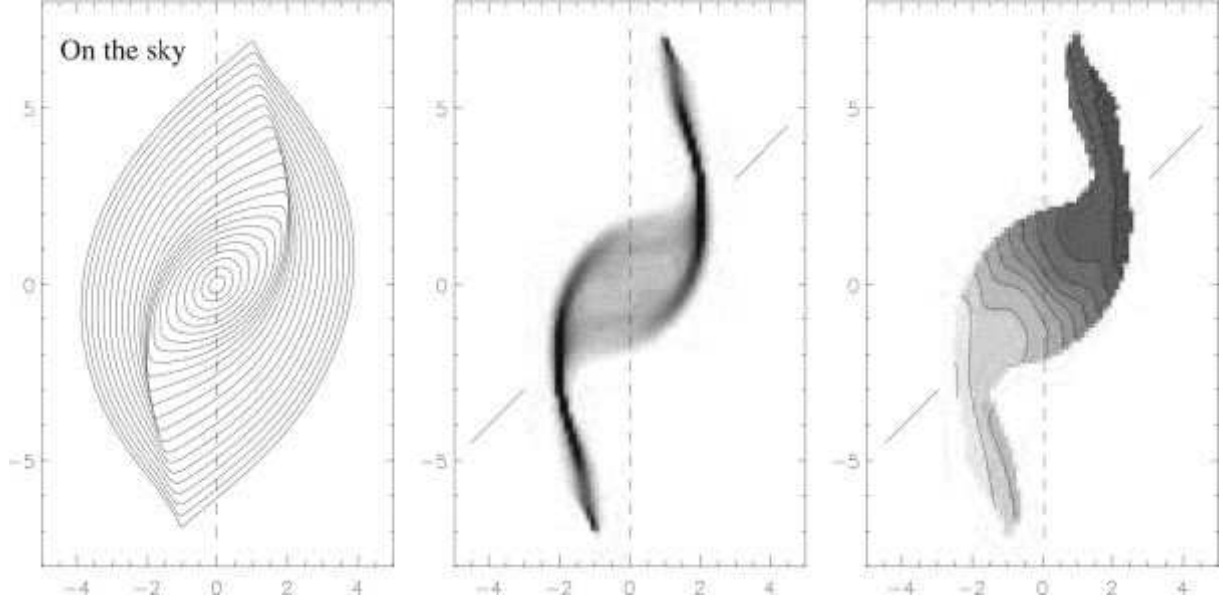


**Fig. 10.** *Left:* Gas orbits in a bar projected on the sky. The position angle and inclination are  $-45^\circ$  and  $30^\circ$ , respectively. We first rotated the gas orbits (Figure 9 *left*) counterclockwise by  $4^\circ$ , so that the bar (dashed line) runs vertically, like that in NGC 4303. *Middle:* Density map, calculated from the gas orbits based on the speed of gas motions. The radial density profile is set to be  $\exp(-r/4)$  for  $r > 2$  and constant for  $r \leq 2$ . We do not show low density regions. The solid lines indicate the major axis (P.A. =  $-45^\circ$ ). *Right:* Velocity field, calculated from the gas orbit model.



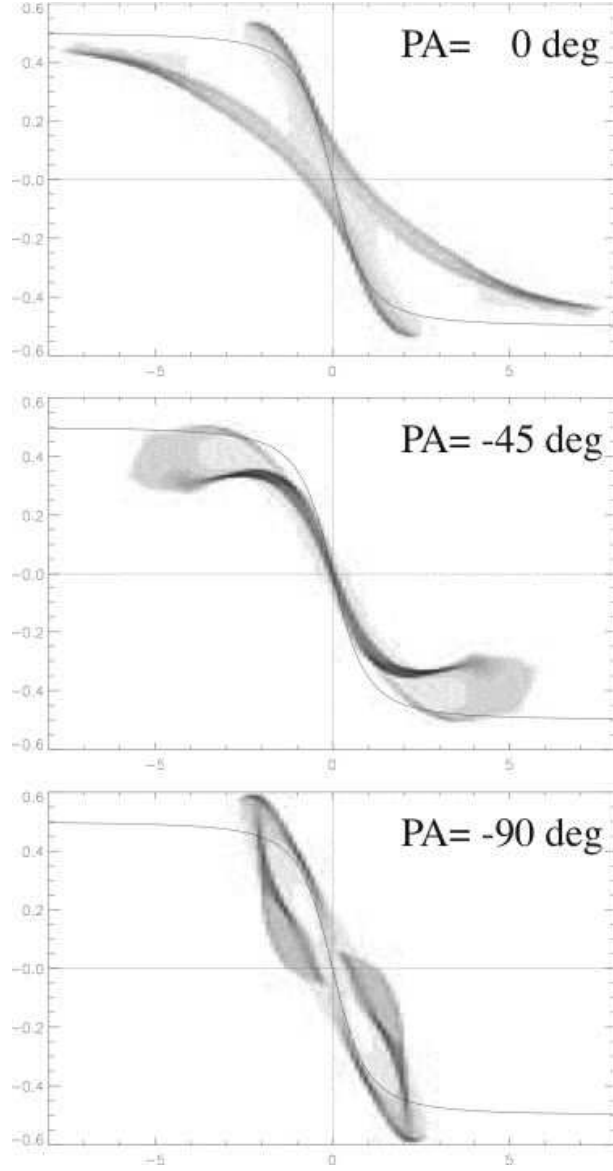


**Fig. 11.** Position-velocity diagrams of the model in Figure 10 observed from the three different position angles, i.e.  $0^\circ$  (*top*),  $-45^\circ$  (*middle*), and  $-90^\circ$  (*bottom*). The diagram with  $PA = -45^\circ$  corresponds to NGC 4303. The same gas distribution shows quite different patterns; our determination of PA fits the data. The solid curves are the rotation curve given by the assumed potential.

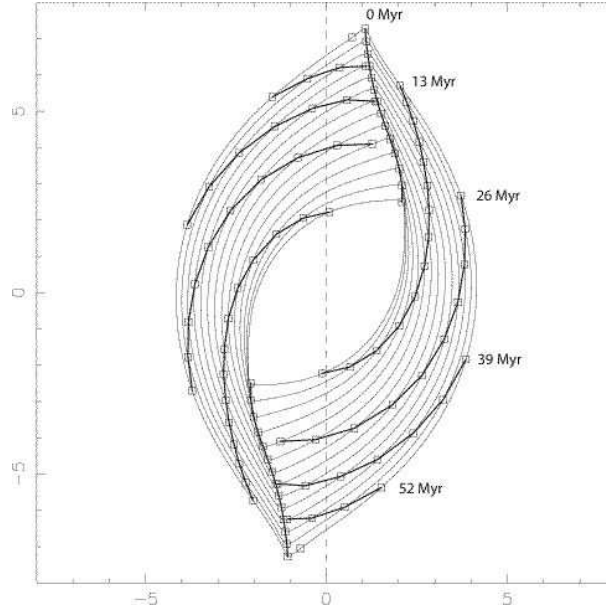


**Fig. 12.** Isochrones of gas flows. The thick solid lines indicate 0, 13, 26, 39, 52 Myr after passage over the turning points (the offset ridges). Gas orbits (same as Figure 9) are also shown for a reference.

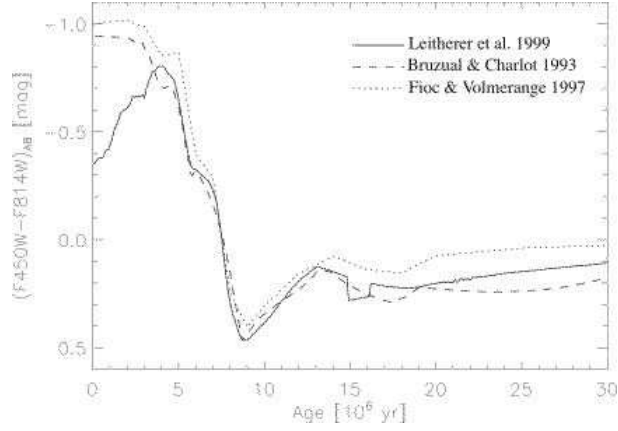


**Fig. 13.** Model color evolution of stellar clusters.

**Table 1.** Parameters of NGC 4303.

Parameter	Value	Reference
Alias	M61	
Hubble type	SAB(rs)bc	1
Nuclear activity	H	2
Distance (Mpc)	16.1	3
Linear scale of 1'' (pc)	78.1	
P.A.(isophotal)		
Inclination (isophotal)		
$V_{\text{sys}}$ (kms $^{-1}$ )	1569	1
$D_{25}^0$ (arcmin)	6.46	1
$B_T^0$ (mag)	10.12	1
$S_{CO(1-0)}(45'')$ (Jy kms $^{-1}$ )	$494 \pm 87$	4
$S_{CO(1-0)}(13'')$ (Jy kms $^{-1}$ )	$193 \pm 6$	5

References: (1) de Vaucouleurs, G. et al. 1991; (2) Ho et al. 1997; (3) Ferrarese et al. 1996; (4) Kenney, Young 1988, 45'' (FWHM) beam centered at  $\alpha_{1950} = 12^{\text{h}}19^{\text{m}}21^{\text{s}}.4$  and  $\delta_{1950} = +4^{\circ}44'58''.0$ ; (5) Nishiyama, Nakai 2001, 16'' (FWHM) beam centered at  $\alpha_{1950} = 12^{\text{h}}19^{\text{m}}21^{\text{s}}.4$  and  $\delta_{1950} = +4^{\circ}44'58''.0$

**Table 2.** Observational parameters.

Parameter	Value
Year	1999 Dec. - 2000 Feb.
Field center	
$\alpha_{1950}, \delta_{1950}$	$12^{\text{h}}19^{\text{m}}21^{\text{s}}.60, +4^{\circ}45'03''.0$
$\alpha_{2000}, \delta_{2000}$	$12^{\text{h}}21^{\text{m}}54^{\text{s}}.97, +4^{\circ}28'24''.9$
Field of view	65''
Array configuration	AB, C, D
Observing frequency	114.65925 GHz
Band width	512 MHz

**Table 3.** Parameters of CO(1-0) cubes.

Parameter	Value	Value
Configuration	AB+C+D	AB+C+D
Weighting	NA	UN
Synthesized beam	$2''.8 \times 1''.9, 166^\circ$	$1''.4 \times 1''.3, 11^\circ$
$\Delta V$ ( $\text{km s}^{-1}$ )	10.4	31.2
rms ( $\text{mJy beam}^{-1}$ )	21	24
$T_b$ for $1 \text{ Jy beam}^{-1}$	17.3	50.5
$T_b$ for $1 \text{ Jy arcsec}^{-2}$	91.9	91.9

**Table 4.** Kinematic parameters of the nuclear disk

Parameter	Value
Dynamical center	
$\alpha_{1950}, \delta_{1950}$	$12^{\text{h}}19^{\text{m}}21^{\text{s}}.67, +4^\circ45'03''.7$
$\alpha_{2000}, \delta_{2000}$	$12^{\text{h}}21^{\text{m}}54^{\text{s}}.94, +4^\circ28'25''.6$
$V_{sys}$ ( $\text{km s}^{-1}$ )	1556.5
P.A. (deg)	-44.45
$i$ (deg)	29.13